The influence of aspect ratio on the determination of tearing energy in mode I fracture tests

E. Kahle [a], A.E. Ehret [a,b], E. Mazza [a,b,*]

[a] *ETH Zurich, Institute for Mechanical Systems, 8092 Zürich, Switzerland*
[b] *Empa, Swiss Federal Laboratories for Materials Science and Technology, 8600 Dübendorf, Switzerland*

ABSTRACT

The energy for tearing is a classical measure of fracture toughness for elastic materials at finite strains. The prominent approach to quantify the tearing energy utilizes a tensile test on edge-cut thin rectangular specimens with low height-to-width ratio to determine the critical stretch at which a crack propagates from the tip of the cut. The analysis of the experiment, proposed by Rivlin and Thomas (1953), relies on the assumption that a large portion of the test piece is in a state of plane strain, and that the change of the total elastic energy is equal to the energy release due to the formation of new crack surfaces. While these assumptions are well justified for test pieces with sufficiently low height-to-width ratio, limitations in the availability and homogeneity of various sample materials have enforced the use of specimens with higher height-to-width ratios. In order to analyse the applicability of the classical theory and the corresponding errors, we investigate in the present work the influence of the sample's height-to-width ratio on the estimation of the tearing energy in mode I fracture tests. Exemplified with experiments and simulations for the elastomer Ecoflex 1:1, we show that reliable measurements can be obtained even for a quadratic sample geometry. For tough materials, however, significant overestimation of the tearing energy is expected already for a height-to-width ratio larger than 1/2. Surprisingly, in very brittle materials the tearing energy is vice-versa prone to be underestimated by up to 10% for ratios up to 1. The error also depends on the non-linear stress–strain characteristics, as illustrated by the use of different constitutive models. While a generally valid geometrical criterion cannot be defined based on the present results, our results suggest that the error hardly exceeds 10% for height-to-width ratios of up to 1/2.

1. Introduction

Natural and synthetic rubber-like materials have a wide range of industrial use [1,2], including various applications with increased safety requirements such as seals, hoses and shock absorbers [3]. Silicone elastomers in particular play an additionally important role in biomedical engineering due to their high chemical stability that allows repeated sterilization and a high degree of "biocompatibility" when interacting with biological tissues [4]. Silicone materials are therefore used both in various extracorporeal medical devices and within the body, e.g. for various orthopaedic and aesthetic implants [4–7]. In view of these pivotal applications, not only the deformation behavior needs to be considered in the design process, but also the critical conditions under which these materials
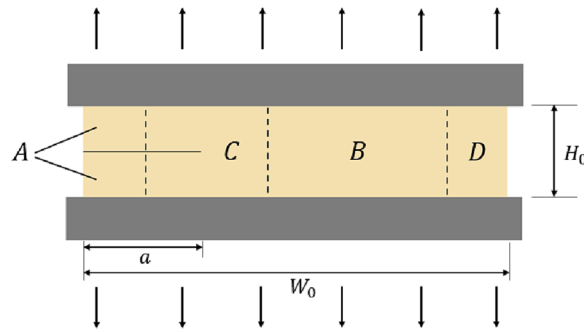
Fig. 1. Schematic of mode I fracture test piece adapted from [10]. Four regions of different deformation state can be distinguished: region A is unloaded, far-field region B is in a pure shear state, region C is in an intricate deformation state, region D is influenced by the free lateral boundary.

potentially fail. Since careful product design generally avoids that these products would be exposed to loads that let them reach their ultimate properties such as strength, it is much more the ability of tolerating small defects that decides on the integrity of the products.

The ability of a material to resist mechanical loads in the presence of a crack-like defect [8] is quantified in terms of the "fracture toughness". While for elastic materials under small strains the latter can be quantified by critical stress intensity factors [9], the typically finite deformations that elastomers undergo in their applications call for alternative metrics. The "characteristic energy for tearing" Γ introduced by Rivlin & Thomas [10] represents the most common one of these metrics and characterises the energy released by fracture of highly deformable hyperelastic materials based on the balance of the deformation energy stored in a sample before and after crack propagation.

Under the assumption of incompressibility, the mode I tearing energy can be determined by means of the "pure shear" tear test [10]. It employs a flat rectangular test specimen with a lateral cut, which is elongated in the direction perpendicular to the cut until crack propagation is observed at the cut tip. The test piece geometry is chosen so that the width W_0 of the test piece is larger than its height H_0, with the intention to generate a large region within the specimen that is in a kinematic state of "pure shear", i.e. a special state of plane strain. This condition is a theoretical prerequisite of the formalism proposed by Rivlin and Thomas [10], and raises the question of critical height-to-width ratios (H_0/W_0) for its application. As discussed in [10,11], such a deformation state occurs in the center region B of the test piece, see Fig. 1, while the stress and deformation fields are heterogenous in the other regions of the sample. Rivlin and Thomas [10] studied samples with H_0/W_0 between 1/15 and 1/5. A detailed analysis in [11] quantified the size of the region affected by the free edge (i.e. region D in Fig. 1) for different applied extensions and H_0/W_0-ratios in a neo-Hookean material. The calculations showed that this region has a width in the order of $1.5H_0$ to $2H_0$ for a strain of 1%, and that the region's width decreases with applied strain. Based on this analysis, a height-to-width ratio below 1/5 was suggested [11]. Other sources in literature provide guidelines on the optimal aspect ratio for mode I specimens [12,13]. For instance, Treloar [12] showed that the contraction in lateral direction is negligibly small compared to the extension in loading direction for a H_0/W_0-ratio of 1/15.

It seems clear that reducing the H_0/W_0-ratio would generally increase the region B and thus improve the estimation of the tearing energy. However, there are several reasons that might limit the aspect ratio in experiments: Increasing the width of the specimen scales the cross-sectional area and thus the axial force in the testing device such that the measurement range of the load cells might be exceeded. Reducing the height instead typically complicates the optical displacement analysis within the gap that remains between the grips, as well as increasing the influence of the clamping conditions and aggravating effects caused by misalignment of the sample and cut. In soft tissues and elastomer samples produced at laboratory scale any increase of the sample size typically goes along with an increased heterogeneity within the sample, and finally it might be the availability of biological samples that limit the dimensions of the corresponding test pieces.

For these and other reasons several authors have used samples with different aspect ratios. For instance, the tearing energy of different silicone elastomers was quantified by use of samples with $H_0/W_0 = 1/6$ [14,15]. Similar and even larger aspect ratios were used to analyse the fracture properties of soft biological tissues [16], and mode I fracture tests on tough hydrogels were performed on samples with aspect ratios in the range from 1/5 to 1/2 [17–23].

While recent work focused on the influence of dissipative material behavior [24] and dynamic crack propagation [25], the present work analyses the onset of crack propagation in elastic materials. We combine experimental results and computational parametric studies to analyse the influence of the test piece geometry on the determination of the tearing energy. The deviation between apparent and effective tearing energy is quantified and its dependence on the test piece geometry is rationalized. Furthermore, we investigate the influence of material brittleness and elastic stress–strain behavior on the range of acceptable height-to-width ratios.

2. Materials & methods

2.1. Theoretical background

In the "pure shear" mode I tear test, a rectangular test piece (width W_0 and height H_0) with a low H_0/W_0-ratio and a lateral pre-cut is elongated in direction perpendicular to the cut plane until crack growth occurs at a particular critical stretch $\lambda_c = h_c/H_0$. The
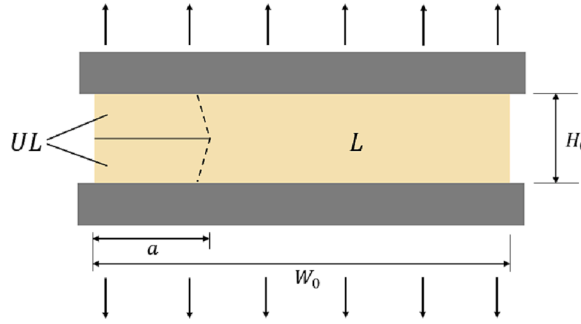
Fig. 2. Schematic of mode I fracture test piece, differentiating between a loaded region L ahead of the crack tip and an unloaded region UL.

elongation of the sample from the initial height H_0 to the critical height h_c is assumed to be an elastic process, in which at each time point all work invested in the deformation of the sample results in elastically stored energy $U = \int_V w \, dV$, with w being the strain energy density (per unit reference volume). The tearing energy is thus determined based on the incremental reduction of the strain energy $U(\lambda_c)$ per increase in fracture surface area $T_0 \, da$ as [10]

$$\Gamma = -\frac{1}{T_0} \frac{dU}{da}\bigg|_{\lambda_c} \tag{1}$$

where T_0 denotes the initial sample thickness. The method, originally proposed by Rivlin and Thomas in [10], considers a far-field region in the test piece (region B in Fig. 1) to be in a state of pure shear deformation. For this region the strain energy density can be determined as the work per reference volume invested in loading a corresponding sample without cut, i.e. the area under the stress-stretch curve of a test piece with width W_0 and height H_0:

$$\overline{w}(\lambda_c) = \int_1^{\lambda_c} P \, d\lambda \tag{2}$$

where $P = F/(W_0 T_0)$ is the first Piola-Kirchhoff stress. Upon advance of the crack by a length increment da, the region C in Fig. 1 is assumed to translate in a self-similar fashion by da "to the right", thus causing a decrease of the volume of the loaded region B by $dV = H_0 T_0 \, da$ and a corresponding increase of the unloaded region A. Thus, a release of strain energy associated with the crack advance da can be quantified as $dU = -\overline{w}(\lambda_c) H_0 T_0 \, da$.

The assumption of a self-similar crack propagation is well justified only for a test piece with low H_0/W_0-ratio. For this reason, we will generally refer to the thus determined tearing energy as the "apparent tearing energy"

$$\Gamma_{app} = -\frac{1}{T_0} \frac{-\overline{w}(\lambda_c) H_0 T_0 \, da}{da}\bigg|_{\lambda_c} = \overline{w}(\lambda_c) H_0 \tag{3}$$

that coincides with the material property Γ only for suitable sample geometries. With increasing H_0/W_0 the pure shear deformation state progressively transitions into a uniaxial deformation state, so that the identification of a rectangular region B with pure shear deformation fails.

In order to generalize the analysis, we propose to consider two regions of the test piece, with reference to Fig. 2: the "loaded region" L and the "unloaded region" UL, distinguished by means of a suitable threshold value of the strain energy density. In general, upon crack propagation by an increment da, the loaded region L undergoes a reduction in volume by dV_L, and the average strain energy density w_L of the loaded region is reduced by dw_L. Hence, the elastic energy U can be represented as a function of the volume V_L and the average strain energy density w_L of the loaded region, and its total differential can be expressed as

$$dU = w_L dV_L + dw_L V_L \tag{4}$$

where the first term marks the contribution of the volume loss from the loaded into the unloaded region, while the second term incorporates the influence of the change in average strain energy density. Consequently, the tearing energy is given as

$$\Gamma = -\frac{1}{T_0} \frac{w_L dV_L + dw_L V_L}{da}\bigg|_{\lambda_c} \tag{5}$$

When comparing Γ to Γ_{app}, we thus obtain

$$\frac{\Gamma}{\Gamma_{app}} = -\frac{w_L \, dV_L + V_L \, dw_L}{\overline{w} \, H_0 T_0 \, da} = \underbrace{\frac{-w_L \, dV_L}{\overline{w} \, H_0 T_0 \, da}}_{\phi'} + \underbrace{\frac{-V_L \, dw_L}{\overline{w} \, H_0 T_0 \, da}}_{\phi''}, \tag{6}$$
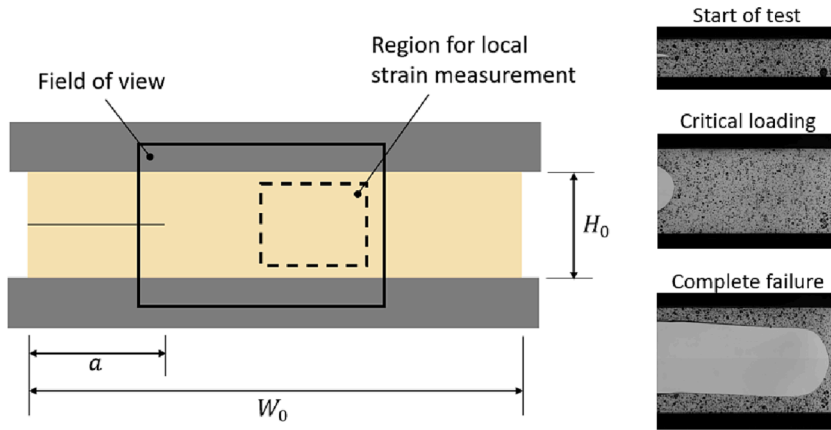
Fig. 3. Left: schematic illustration of the mode I fracture test. In the center of the field of view (solid square), a small zone (dashed square) is considered to determine the local stretch in loading direction λ. Right: top-view images of a sample at the beginning (top) of a test, at critical loading (middle) and immediately before complete failure (bottom).

where $\Gamma = \Gamma_{app}$ implies $\phi' + \phi'' = 1$, and indeed Rivlin and Thomas' theory [10] assumes $\phi' = 1$ and $\phi'' = 0$. Deviations of Γ_{app} from Γ arise as a consequence of (i) ϕ' being different from 1, and (ii) ϕ'' being different from 0. It is well-known and also confirmed by our results presented herein that for samples with small aspect ratio, i.e. $H_0 \ll W_0$, $\overline{w} \approx w_L$, $dV_L \approx H_0 T_0 da$ and $dw_L \approx 0$, so that $\Gamma_{app} \approx \Gamma$. However, Eq. (6) is more general and shows that the exact value of Γ can be obtained even if the criterion of self-similarity does not hold, if ϕ' compensates a non-zero ϕ''-value. In Section 3.4, we will analyse the influence of the terms ϕ' and ϕ'' for different aspect ratios H_0/W_0.

2.2. Sample preparation

Experiments were performed on Ecoflex (Smooth-On, USA), which is known to display markedly elastic behavior [26], so that potential dissipative effects affecting the determination of the tearing energy according to Eq. (3) could be neglected. Ecoflex samples were prepared by mixing two parts A and B in a 1:1 wt ratio [27]. Ecoflex with a hardness of Shore 00 30 was chosen, which has a curing time of 4 h. The mixture was stirred continuously, vacuumed in a vacuum chamber and clamped between two glass plates, separated by strips of insulation tape, to cure for at least 12 h at room temperature.

For fracture tests, rectangular samples were cut from the cured Ecoflex sheets. Five different free sample heights H_0 of 6 mm, 30 mm, 60 mm, 120 mm and 240 mm were chosen, while $W_0 = 60$ mm for all samples, thus giving rise to aspect ratios from 1/10 to 4. A lateral edge cut of $a = 20$ mm length was added with a scalpel. Note that the total sample height before clamping is $H_0 + 20$ mm in order to provide sufficient clamping area. Additionally, samples without cut ($a = 0$ mm) were tested to determine a reference stress-stretch curve, from which $\overline{w}$ was determined according to Eq. (2) for each value of H_0.

The characterization of the deformation behavior of Ecoflex used data from unnotched samples with $H_0 = 6$ mm and $W_0 = 60$ mm (referred to as pure shear state PS), from test pieces with $H_0 = 40$ mm height and $W_0 = 10$ mm width (uniaxial stress state UA), and equibiaxial stress state (EB). For the latter, inflation tests were performed, using circular samples with diameter 70 mm (free diameter $D_0 = 50$ mm). To allow for optical deformation analysis a trackable pattern of black marks was sprayed on the specimen surface with a graphite spray (Kontakt Chemie Graphit 33 Spray).

Before testing, the initial thickness T_0 of each sample was determined as the averaged value measured at three different positions, using a microscope in brightfield mode (LSM 5 Pascal, Carl Zeiss GmbH, Jena, Germany) with a measurement precision in the order of 0.01 mm [28].

2.3. Experimental testing and analysis

One axis of a custom-built horizontal biaxial testing setup (MTS Systems, Eden Prairie, MN, USA, force range: 100 N) was used for uniaxial tension (UA), pure shear (PS) and mode I fracture tests [29–31]. The setup consists of hydraulic actuators equipped with force sensors, and a CCD camera system (Pike F-100B Allied Vision Technologies GmbH, Stadtroda, Germany) with a 0.25 × telecentric lens (NT55–349; Edmund Optics GmbH, Karlsruhe, Germany), allowing to simultaneously record top view images, force (F) and clamping displacement (Δu) signals. Samples were clamped by use of flat metal grips, which had a corrugated strip of sandpaper added on both faces to reduce slippage and which were fastened by screws. 3D-printed inserts were added at the bottom of the grips to ensure parallel alignment of the grip faces. Displacement and force signals were monitored at 10 Hz in UA, PS and fracture tests, while images were recorded at 2 Hz for free sample heights $H_0 = 6$ mm, at 6 Hz for $H_0 = 30$ mm, at 10 Hz for $H_0 = 40$–60 mm and at the maximum sampling rate of 20 Hz for $H_0 \geq 120$ mm.

UA, PS and mode I fracture tests were performed at a nominal strain rate of 1/min. The camera's field of view was placed in the

central area, so that it included the cut tip for notched specimens, as shown in Fig. 3. The force signal provided by the force sensors and the clamping displacement Δu of the grips were recorded, providing the force F and current nominal gauge length h, respectively. For the unnotched test pieces, the nominal stress was obtained by relating the force to the initial cross-sectional area as $P = F/(W_0 T_0)$. Data analysis of samples was based on a small, specified force threshold [32] of 0.05 N, reached at a sample height H_{ref}. Nominal stretch in loading direction was thus $\lambda_N = h/H_{ref}$. Note that the difference between H_{ref} and H_0 was generally very small, with H_{ref}/H_0 was ≤ 1.05 for all test pieces. The local in-plane stretches λ (in loading direction) and λ_2 (perpendicular to loading direction) were obtained using a custom optical flow based strain measurement technique [28], which tracks features on the sample surface in a specified rectangular zone of acquired top view images and reconstructs the homogenized in-plane strain field. For fracture samples, this zone was set at sufficient distance from both the cut tip and the free edge of the sample. The strain energy density $\overline{w}(\lambda)$ in Eq. (2) was determined through numerical integration of the reference stress-stretch curve extracted from the response of unnotched specimens with corresponding H_0/W_0-ratios. Local stretch measurements were used for that purpose, such that the area under the stress-stretch curve is not affected by slippage at the clamps. For fracture samples, the instance of crack propagation was determined by visually analysing the top view image series and quantifying the corresponding failure stretch λ_c from the image, in which crack advance was detected. Since λ_c is based on local stretch data, it is not influenced by slippage [14]. Following modifications [15] of the classical equation [10] (Eq. (3)), the tearing energy was determined as $\Gamma = \gamma_c H_0 \int_1^{\lambda_c} P d\lambda$, where γ_c is a factor that is given through the ratio of nominal and local stretch at crack propagation, and accounts for potential slippage of the test piece in the clamps [15]. Cauchy stresses in UA and PS tests were computed in terms of the force and current cross-sectional area with $\sigma = \lambda F/(W_0 T_0)$, applying the assumption of incompressibility $\lambda_2 \lambda_3 = 1/\lambda$.

Inflation tests were performed by means of a custom built setup [29,31,32], in which circular samples are clamped between the inflation cylinder and a cover ring with inner diameter $D_0 = 50$ mm, and fastened by screws. The samples are inflated by pumping air into the aluminium cylinder with a syringe pump (Standard Infuse/Withdraw PHD Ultra Syringe Pumps, Harvard Apparatus, Holliston, MA, USA), controlled by a custom LABVIEW (National Instruments, Huntsville, AL, USA) code. Pressure is measured with a pressure sensor (digital manometer, LEX 1, Keller, Switzerland), and two CCD cameras (GRAS-14S5C-C, Point Grey, Richmond, BC, Canada) recorded top and side view images at 1 Hz. For the present experiments, samples were loaded in a volume-controlled manner by pumping 2.5 mbar min^{-1} of air into the cylinder up to 8 mbar. Local in-plane stretches λ_1 and λ_2 were computed from top view images [28], and the curvature of the sample was determined from side view images by means of an in-house Python algorithm [28]. From the measured pressure p, the radius of curvature r at the apex and the current thickness $\lambda_3 T_0$, the Cauchy stress was calculated as $\sigma = pr/(2\lambda_3 T_0)$, where the stretch in thickness direction is given as $\lambda_3 = 1/(\lambda_1 \lambda_2)$ due to incompressibility.

2.4. Computational material models

Following [33], Ogden's material model was adopted for Ecoflex, so that the strain energy density function in terms of the principal stretches $\Lambda_1, \Lambda_2, \Lambda_3$ is given as [34]

$$w(\Lambda_1, \Lambda_2, \Lambda_3) = \sum_{i=1}^{N} \frac{\mu_i}{\alpha_i} \left(\Lambda_1^{\alpha_i} + \Lambda_2^{\alpha_i} + \Lambda_3^{\alpha_i} - 3 \right),$$

with $N = 3$, and material constants μ_i, α_i.

This incompressible constitutive model was fitted to the average stress-stretch response obtained in UA and PS experiments, using sample geometries with a H_0/W_0-ratio of 4/1 and 1/10, respectively. The fitting performed in Abaqus (Abaqus 6.14, DS Simulia Corp., Providence RI, USA) yielded $\alpha_1 = 1.7546$, $\alpha_2 = 2.2439$, $\alpha_3 = 1.2156$, $\mu_1 = -5.8817 \times 10^{-1}$ MPa, $\mu_2 = 2.1038 \times 10^{-1}$ MPa, $\mu_3 = 5.0244 \times 10^{-1}$ MPa.

For comparison, a material model representative for the behavior of soft collagenous tissues was considered. To this end, the constitutive equations proposed in [16] for the bovine Glisson's capsule (GC) were implemented for Finite Element (FE) simulations of mode I fracture tests. The model is based on a hyperelastic anisotropic framework [32,35,36], which considers n = 32 families of fibers uniformly distributed in the plane, with a small out-of-plane inclination $\pm\vartheta$. The fibers are embedded in a highly compliant, compressible matrix and experience an affine fiber stretch $\lambda_i^f, i = 1, 2, \cdots, n$, in the deformed configuration.

The strain energy density is determined as $w = \mu_0 (e^{qg} - 1)/(2q)$, with [32,36]

$$g = m_2 (\mathrm{tr}\, \mathbf{b} - 3) + \frac{m_2}{m_5} \left(J^{-2m_5} - 1 \right) + \frac{\overline{m}_3}{m_4} \frac{1}{N} \sum_{i=1}^{n} \left\langle \lambda_i^f - 1 \right\rangle^{2m_4},$$

where $\mathbf{b}$ denotes the left Cauchy-Green tensor, $J^2 = \det \mathbf{b}$ is its determinant, and $\langle \ldots \rangle$ represent Macaulay brackets, which only allow for contributions of fibers under tension. The model parameters are given as $\mu_0 = 4.78$ N/mm^2, $m_2 = 5.07 \times 10^{-3}$, $\overline{m}_3 = 9.94$, $m_4 = 1.00001$, $m_5 = 0.90$, $q = 6.15$, $\vartheta = 5.77 \times 10^{-2}$ [rad]. The material model was implemented through a user material subroutine in Abaqus.

Computations were performed with the FE software Abaqus (Abaqus 6.14, DS Simulia Corp., Providence RI, USA), using three-node plane stress elements (CPS3). To determine the actual tearing energy Γ according to Eq. (1), crack opening simulations [37,38] were performed to compute the strain energy release rate. Since symmetry along the y-direction can be assumed, only one half of the respective sample was simulated to reduce the computational cost, see Fig. 4. Nodes on the symmetry line were tied in y-direction, the sample was stretched to a given λ, with the non-linear geometry option activated, and the tie constraint of each node on the symmetry
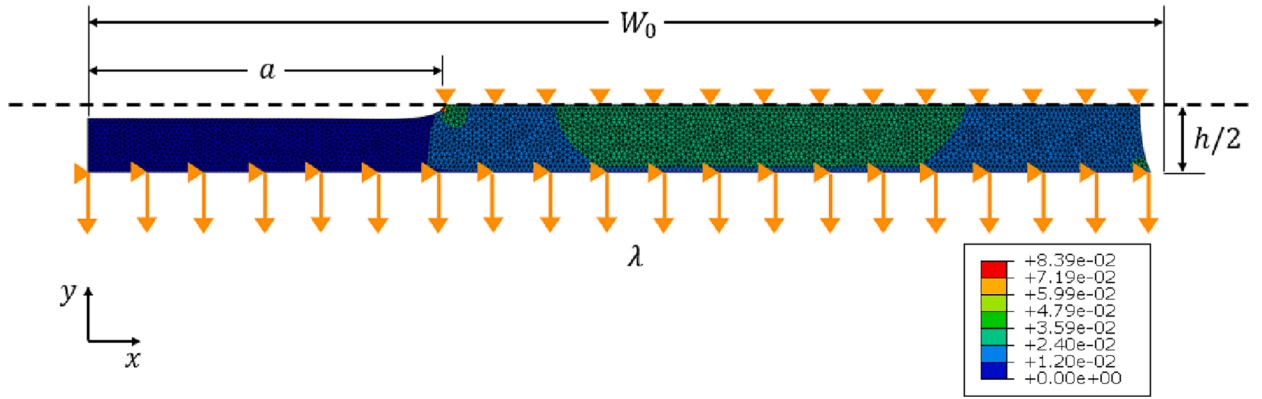
Fig. 4. FE contour plot of maximum principal Cauchy stress ($\sigma_{\text{prin}}^{\text{max}}$) distribution within a mode I fracture test piece. The sample is shown for a stretch of $\lambda = 1.26$, so that the presence of the notch is visible. Geometric dimensions and prescribed boundary conditions are indicated. The dashed black line denotes the line of symmetry.
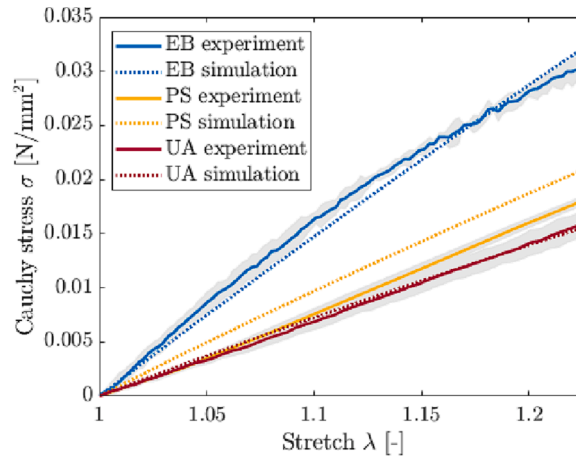

Fig. 5. Cauchy stress vs. stretch from UA, PS and EB experiments (solid lines) and simulations (dashed lines).
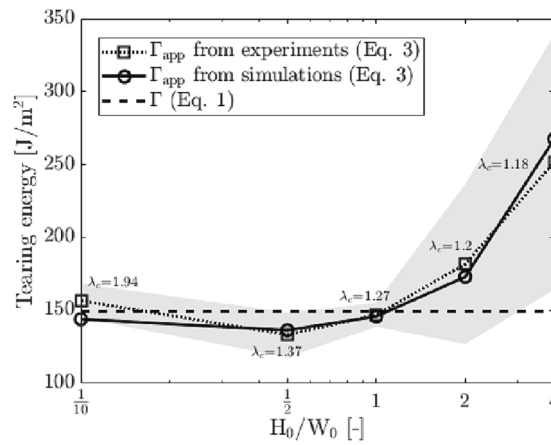

Fig. 6. Apparent tearing energy from experiments (square symbols) and simulations (circle symbols) over H_0/W_0-ratio. The straight dashed black line denotes the reference value $\Gamma = 150$ J/m^2.

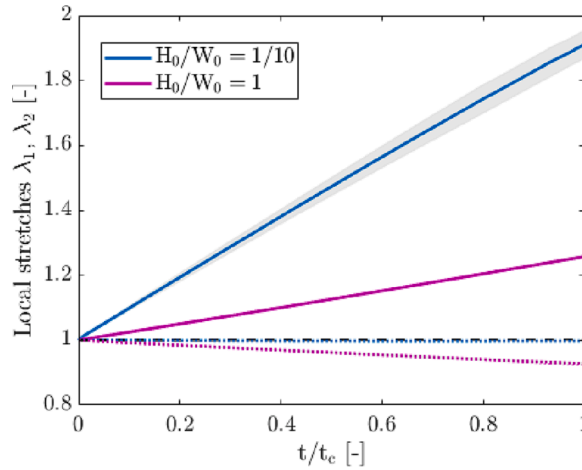**Fig. 7.** Stretches measured in the far-field in loading (λ_1) and lateral (λ_2) direction over the relative time up to onset of crack propagation (at t_c).
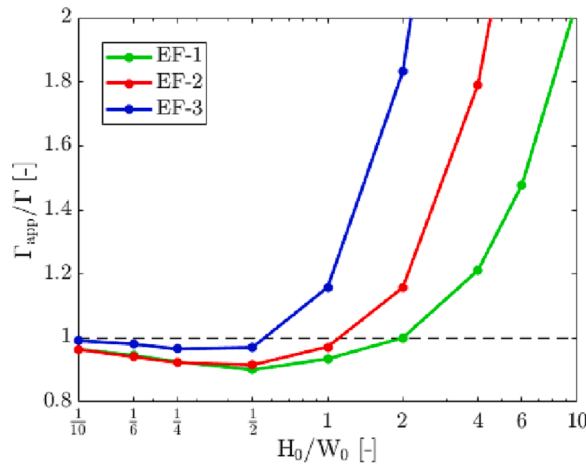

Fig. 8. Γ_{app}/Γ over H_0/W_0 for sets of Ecoflex (EF-1, EF-2, EF-3).

line was subsequently released, such that the crack increased by a length increment $\Delta a = 0.25$ mm. From the corresponding change in elastic deformation energy ΔU and the initial sample thickness T_0, the strain energy release rate for samples with initial crack length a = 20 mm was computed for different initial height-to-width ratios and values of λ with

$$G^{H_0/W_0}(\lambda) = -\frac{1}{T_0} \frac{\Delta U}{\Delta a}\bigg|_\lambda \tag{7}$$

The 'true' tearing energy $\Gamma = G^{1/10}\left(\lambda_c^{1/10}\right) = 150 \, \text{J/m}^2$ of Ecoflex was obtained as the value of G at the experimentally determined fracture stretch $\lambda_c^{1/10} = 1.94$ obtained in mode I fracture tests on samples with aspect ratio $H_0/W_0 = 1/10$ (see Section 3.1). For the computation of all other aspect ratios, the critical stretches $\lambda_c^{H_0/W_0}$ necessary to reach Γ were iteratively determined as

$$\lambda_c^{H_0/W_0} = \left\{ \lambda \,|\, G^{H_0/W_0}(\lambda) \approx \Gamma \right\} \tag{8}$$

through linear interpolation between values of $G^{H_0/W_0}(\lambda)$ at different λ.

By analysis of the FE models at the corresponding $\lambda_c^{H_0/W_0}$, the unloaded sample region (UL in Fig. 2) was specified as the region with an energy density of less than 10% of the average strain energy density $\overline{w}$ at $\lambda_c^{H_0/W_0}$, while the loaded region comprises the rest of the sample. In order to evaluate Eq. (6), the change in volume dV_L of the loaded region was calculated upon advance of the crack by a length increment da = 0.25 mm, and dw_L was obtained from comparison of the average strain energy density within the loaded region before and after crack advance. A larger length increment da = 5 × 0.25 mm was chosen for the generation of certain plots (Fig. 9 and Fig. 10) to achieve more pronounced contributions of dV_L and dw_L. The local strain energy density $w(x)$ (Fig. 11 and Fig. 14) was
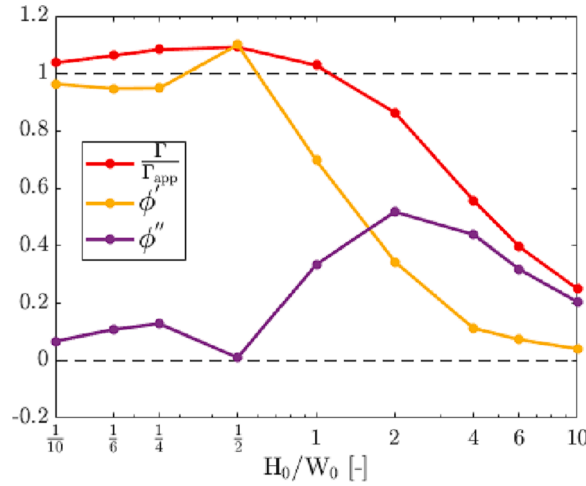
Fig. 9. Terms ϕ' and ϕ'' over H_0/W_0 for set of Ecoflex EF-2 (here: da $= 5 \times 0.25$ mm). The ratio Γ_{app}/Γ is shown as the inverse (in red) for the sake of simplicity.
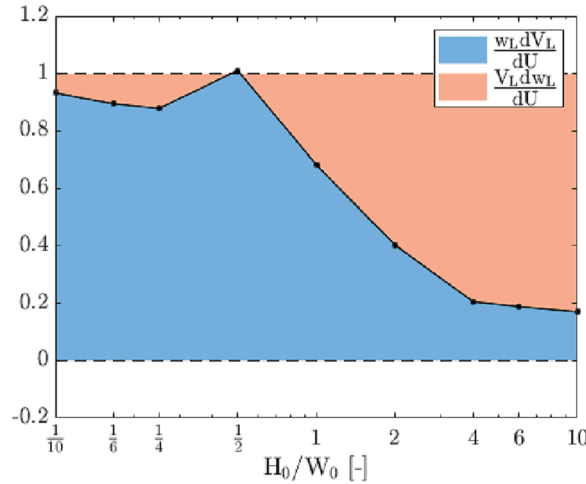

Fig. 10. Ratios $\frac{w_L dV_L}{dU}$ and $\frac{V_L dw_L}{dU}$ over H_0/W_0 for set of Ecoflex EF-2 (here: da $= 5 \times 0.25$ mm). dU is the decrease in total strain energy upon crack advance by da.

directly exported from Abaqus as an element output variable.

2.5. Parametric study

Nine different H_0/W_0-ratios (1/10, 1/6, 1/4, 1/2, 1, 2, 4, 6 and 10) were simulated by use of samples with fixed width $W_0 = 60$ mm and initial heights H_0 from 6 mm up to 600 mm. Identical FE discretization was ensured for all ratios for the sake of comparability.

Based on the reference value of $\Gamma = 150$ J/m^2, the fracture mechanics-based predictions of λ_c for various initial H_0/W_0-ratios were obtained as follows: using a custom Matlab algorithm energy release rates were calculated based on crack opening simulations for different λ. From the range of obtained values $G^{H_0/W_0}(\lambda)$, the critical stretch $\lambda_c^{H_0/W_0}$ was iteratively determined according to Eq. (8). The results formed the basis for the assessment of the difference between Γ and Γ_{app} for Ecoflex test pieces of different H_0/W_0-ratios.

For a subsequent parametric study, calculations were also performed assuming a much lower (set EF-1), as well as a much higher (set EF-3) fracture toughness than that determined for Ecoflex (set EF-2), viz. Γ-values of 0.030 J/m^2 and 2700 J/m^2, see Table 1.

A similar procedure was adopted for GC, whereby besides the actual tearing energy of $\Gamma = 2700$ J/m^2 corresponding to the experimentally determined fracture stretch $\lambda_c^{1/6} = 1.2$ reported for samples with $H_0/W_0 = 1/6$ [16], a second and much lower hypothetical tearing energy $\Gamma = 2.4$ J/m^2 was studied, corresponding to a stretch $\lambda_c^{1/10} = 1.01$ in samples with $H_0/W_0 = 1/10$.

The apparent tearing energy according to Rivlin & Thomas [10] was calculated for all H_0/W_0-ratios through numerical integration of the simulated stress-stretch curves from corresponding intact samples up to λ_c, using Eq. (3). To compare Γ_{app} with Γ, the ratio Γ_{app}/Γ
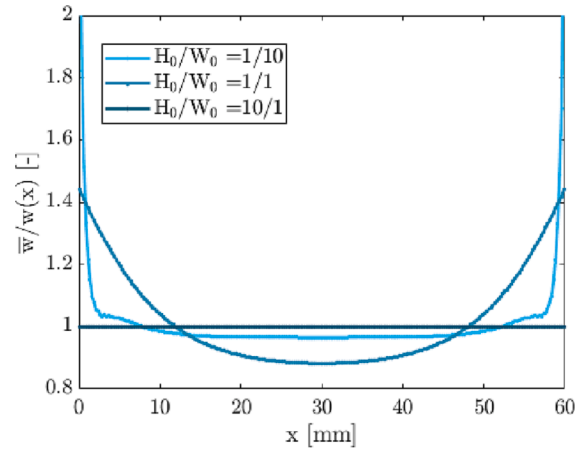
Fig. 11. Ratio between mean strain energy density $\overline{w}$ and local strain energy density $w(x)$ vs. x-distance from free edge for the set of Ecoflex EF-1 with a H_0/W_0-ratio of 1/10, 1 and 10.
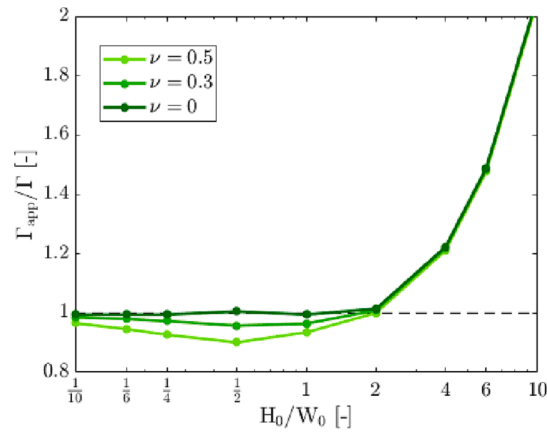

Fig. 12. Γ_{app}/Γ over H_0/W_0 for a linear elastic material equivalent to set of Ecoflex EF-1 with a Poisson's ratio ν of 0.5, 0.3 and 0.
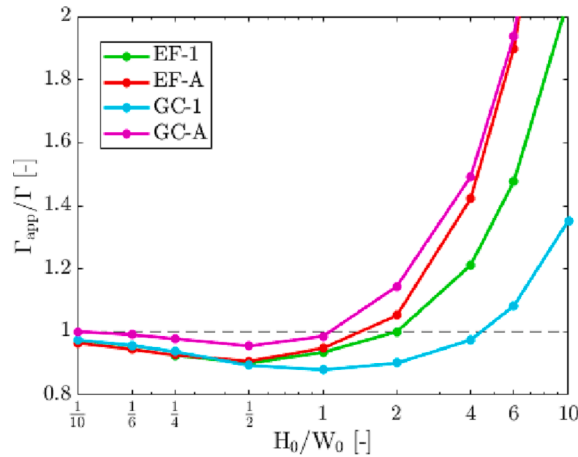

Fig. 13. Γ_{app}/Γ over H_0/W_0 for sets of Ecoflex (EF-1, EF-A) and Glisson's capsule (GC-1, GC-A).

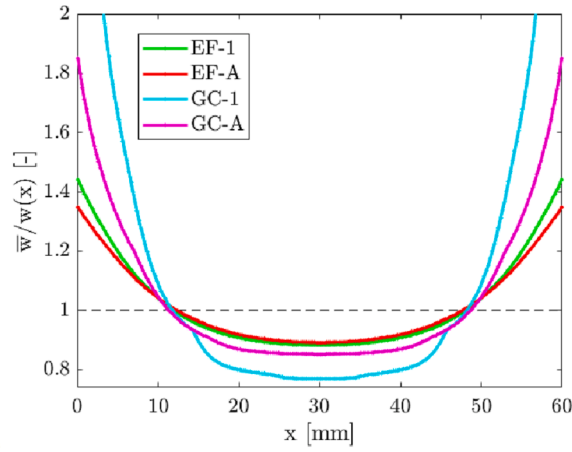**Fig. 14.** $\overline{w}/w(x)$ vs. x-distance from free edge for sets of Ecoflex (EF-1, EF-A) and Glisson's capsule (GC-1, GC-A) with $H_0/W_0 = 1$.
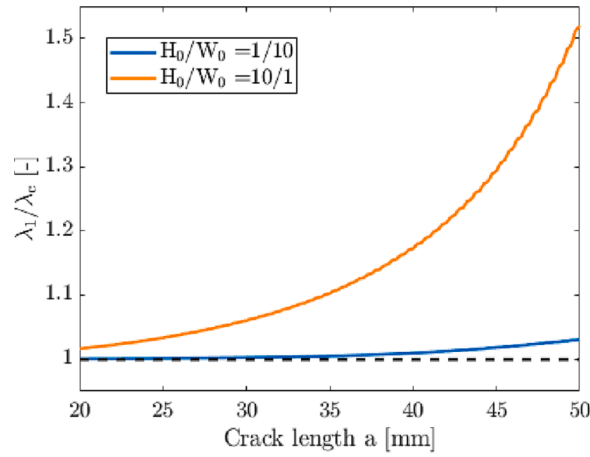

Fig. 15. Calculated far-field stretch λ_1 over the critical stretch λ_c as a function of crack length. Note the fairly constant value of the far-field stretch for the case of the short test piece, while the case of large aspect ratio leads to a pronounced dependence on crack size.
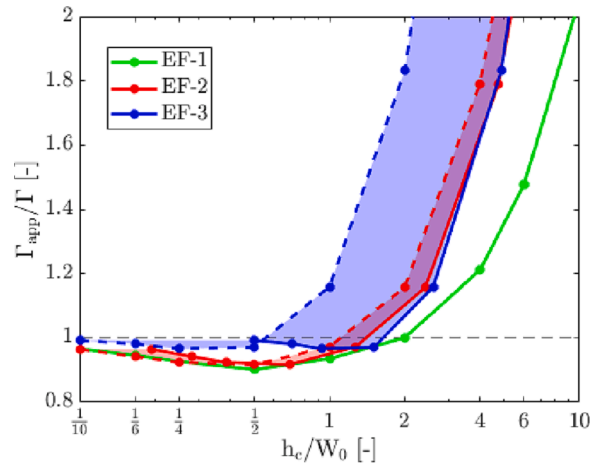

Fig. 16. Γ_{app}/Γ over current h_c/W_0-ratio (solid line) for sets of Ecoflex EF-1, EF-2 and EF-3. Γ_{app}/Γ over the initial H_0/W_0-ratio is shown as dashed lines, and the area between the ratios for each set is shaded to visualize the shift in Γ_{app}/Γ from the reference to the deformed configuration.

Table 1

Γ-values for parameter sets of Ecoflex (EF-1, EF-A, EF-2, EF-3) and Glisson's capsule (GC-1, GC-A).

	Ecoflex				GC	
	Set EF-1	Set EF-A	Set EF-2	Set EF-3	Set GC-1	Set GC-A
Γ [J/m^2]	0.030	17	150	2700	2.4	2700

Table 2

Fracture stretches λ_c for different H_0/W_0-ratios resulting in respective Γ-value for parameter sets of Ecoflex (EF-1, EF-A, EF-2, EF-3) and Glisson's capsule (GC-1, GC-A).

		Ecoflex				GC	
	H_0/W_0	Set EF-1	Set EF-A	Set EF-2	Set EF-3	Set GC-1	Set GC-A
Γ [J/m^2]	–	0.030	17	150	2700	2.4	2700
λ_c [–]	1/10	1.0100	1.2642	1.9398	5.0000	1.0100	1.2327
	1/6	1.0078	1.2000	1.6934	4.2451	1.0078	1.2000
	1/4	1.0064	1.1613	1.5477	3.7147	1.0064	1.1742
	1/2	1.0046	1.1145	1.3796	3.0130	1.0046	1.1357
	1	1.0034	1.0847	1.2763	2.6006	1.0034	1.1073
	2	1.0025	1.0635	1.2109	2.4323	1.0027	1.0894
	4	1.0020	1.0523	1.1849	2.3833	1.0022	1.0780
	6	1.0018	1.0494	1.1790	2.3691	1.0019	1.0744
	10	1.0016	1.0477	1.1748	2.3584	1.0017	1.0736

was calculated, so that any ratio different from one indicates that the assumptions leading to Eq. (3) are not fully satisfied.

2.6. Statistical analysis

Data were analysed using Matlab (Version R2018b, TheMathWorks Inc., Natick, MA, USA). Experimental values in the present study are expressed as mean ± standard deviation.

3. Results

3.1. Experimental deformation behavior and energy for tearing

Fig. 5 compares the stress-stretch curves obtained from experiments and simulations for uniaxial (UA), pure shear (PS) and equibiaxial (EB) loading. The reasonable agreement between experiments and simulations confirms the validity of the constitutive model.

The apparent tearing energy Γ_{app} experimentally determined in mode I fracture tests on Ecoflex samples with an aspect ratio of $H_0/W_0 = 1/10$ using Eq. (3) amounts to $156.6 \, \text{J/m}^2 \pm 11.8 \, \text{J/m}^2$, and thus well matches the reference value of $\Gamma = 150 \, \text{J/m}^2$ obtained in crack opening simulations.

Fig. 6 plots the apparent tearing energy Γ_{app} determined in mode I fracture experiments and corresponding simulations on Ecoflex using Eq. (3). The excellent agreement between simulations and measurements confirms the reliability of both, the FE model and the procedure for determination of critical loading conditions from the numerical analysis. The deviation of Γ_{app} from the reference value of $\Gamma = 150 \, \text{J/m}^2$, shows that Eq. (3) leads to an overestimation of the tearing energy for H_0/W_0-ratios larger than 1 for Ecoflex. For lower ratios, the tearing energy is reasonably described through the procedure of Rivlin & Thomas [10].

A state of pure shear deformation is a prerequisite for the procedure proposed in [10]. Thus, the magnitude of lateral contraction represents an important characteristic of the test configuration. For two test piece geometries Fig. 7 reports the principal stretches measured in the far field (see Fig. 3) in the course of the tests, up to the onset of crack propagation at time t_c. While the case of low aspect ratio confirms the absence of lateral contraction, quadratic samples ($H_0/W_0 = 1$) display significant deviations from a pure shear deformation state. In fact, the lateral strain is close to 50% of the value expected for a uniaxial stress state. Interestingly, despite this violation of the plane strain condition for this case the apparent tearing energy is still very close to the correct value (see Fig. 6).

3.2. Influence of aspect ratio and tearing energy magnitude

Table 2 reports the computed values of the critical stretch λ_c obtained by crack opening simulations for different assumed values of Γ. Set EF-2 reflects the true fracture behavior of Ecoflex with a tearing energy of 150 J/m^2. Moreover, set GC-A represents the fracture toughness determined in [16] for the bovine liver capsule. In order to facilitate the comparison, set EF-A was included for Ecoflex leading to a similar critical stretch as for GC-A.

The reliability of tearing energy determination depends on its magnitude, as shown in the following parametric study. Fig. 8 depicts the ratio Γ_{app}/Γ extracted from FE simulations considering the cases EF-1, EF-2 and EF-3 (see Table 2), over nine different initial

Fig. A1. Maximal principal first Piola-Kirchhoff stress vs. horizontal distance r from crack tip ($a = 20\,\text{mm}$) in the reference configuration for Ecoflex at critical loading conditions.
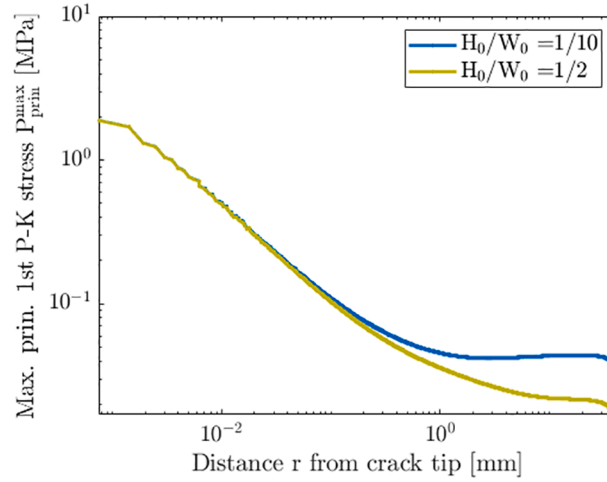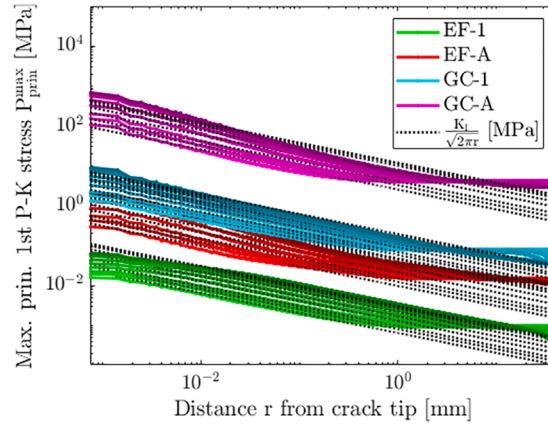

Fig. A2. Maximal principal first Piola-Kirchhoff stress vs. horizontal distance r from crack tip ($a = 20\,\text{mm}$) in the reference configuration for sets of Ecoflex (EF-1, EF-A) and Glisson's capsule (GC-1, GC-A). The dashed lines with slope $-1/2$ represent a stress distribution proportional to $r^{-1/2}$.

Fig. A3. Maximal principal nominal strain vs. horizontal distance r from crack tip ($a = 20\,\text{mm}$) in the reference configuration for sets of Ecoflex (EF-1, EF-A) and Glisson's capsule (GC-1, GC-A). The dashed lines with slope $-1/2$ represent a strain distribution proportional to $r^{-1/2}$.
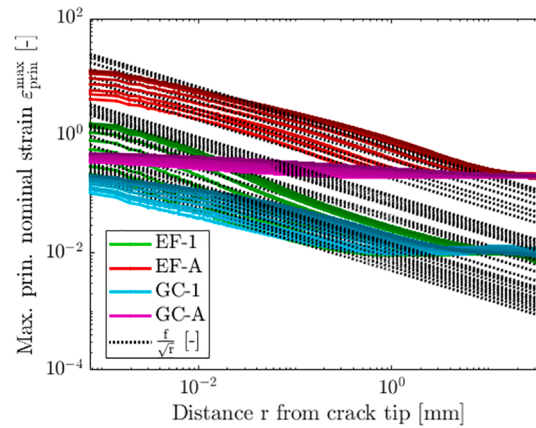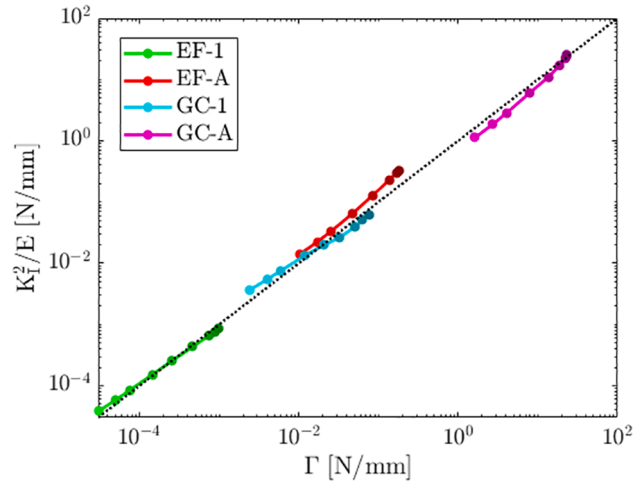
Fig. A4. Tearing energy predicted through stress intensity factor K_I vs. energy release rate Γ for sets of Ecoflex (EF-1, EF-A) and Glisson's capsule (GC-1, GC-A) at different H_0/W_0 between 1/10 and 10 (denoted by dot symbols). Note that H_0/W_0 increases from the left to the right for each curve, visualized by the darker dot symbols. The dashed line with slope one is given to guide the eye.
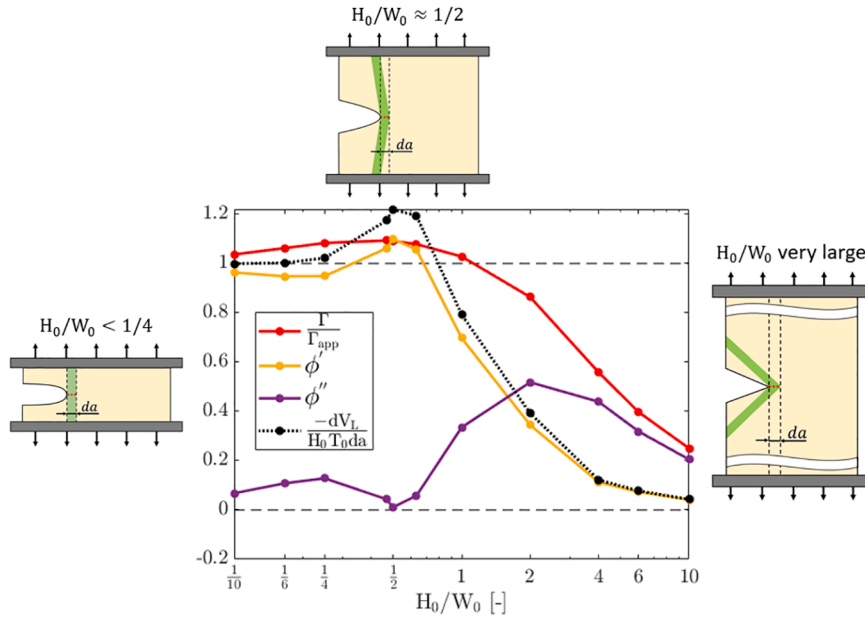

Fig. A5. Terms ϕ' and ϕ'' over H_0/W_0 for Ecoflex set EF-2 (here: da $= 5 \times 0.25$ mm). The ratio Γ_{app}/Γ is shown as the inverse (in red). The relative volume reduction $\frac{-dV_L}{H_0 T_0 da}$ of the loaded region is indicated by the dotted black line. Sketches illustrate for different aspect ratios the unloaded region associated with a crack propagation by da (red dashed line). For low aspect ratios (left), the volume increment of crack growth $H_0 T_0 da$ (dashed black rectangle) and the unloaded volume dV_L (green shaded area) correspond. For very high aspect ratios (right), dV_L is much smaller than $H_0 T_0 da$. For close-to-quadratic sample geometries (middle), dV_L surpasses $H_0 T_0 da$.

H_0/W_0-ratios ranging from 1/10 to 10. Note that EF-1 was selected to mimic brittle material behavior, with $\lambda_c^{1/10} = 1.01$ for the smallest H_0/W_0-ratio. At large H_0/W_0-ratios, Γ_{app}/Γ increases for all sets, which implies an overestimation of the effective tearing energy Γ. For the brittle material, i.e. EF-1, H_0/W_0-ratios up to 2 are still close to 1, even if there is a non-negligible underestimation of Γ for $1/4 < H_0/W_0 < 1$. For higher fracture toughnesses (EF-3), ratios of up to 1/2 lie in tolerable proximity to 1 and thus might be considered acceptable.

3.3. Analysis of the results

Eqs. (5) and (6) are now considered in order to rationalize the results of Fig. 8. Specifically, the two terms ϕ' and ϕ'' are evaluated

for the case EF-2 and represented along with Γ_{app}/Γ in Fig. 9. The overestimation of Γ_{app} for large H_0/W_0-ratios can be explained by the fact that this quantity is determined under the assumption that the decrease in total strain energy dU stems from a volume reduction dV_L of the loaded region by $H_0 T_0 da$, while the strain energy density $w_L = \overline{w}$ in the loaded sample region remains constant during crack advancement. When plotting the first term ϕ' of Eq. (6) (yellow curve in Fig. 9), it becomes visible that a correspondence between the two quantities is only confirmed for H_0/W_0-ratios up to $1/2$. For large ratios, the overestimation of Γ is due to the fact that dV_L is much lower than $H_0 T_0 da$. Furthermore, w_L changes during crack propagation, leading to a contribution $V_L dw_L$ in the change of the total strain energy. The ratio ϕ'' between $V_L dw_L$ and the prediction $\overline{w} H_0 T_0 da$, shown in purple in Fig. 9, displays an almost negligible contribution for low H_0/W_0-ratios, but an increasing influence for ratios of 1 and higher. Interestingly, this second term ϕ'' provides a compensation for the effect of the first term ϕ' for ratios up to 1, see also Fig. A5 in the Appendix.

The contributions of the two terms of the total differential of the strain energy according to Eq. (4) are plotted as the ratios $\frac{w_L dV_L}{dU}$ and $\frac{V_L dw_L}{dU}$ in Fig. 10. The black line corresponds to the ratio $\frac{w_L dV_L}{dU}$ and the difference $1 - \frac{w_L dV_L}{dU}$ represents the second term. The corresponding fractions taken by the two terms are illustrated in blue and orange, respectively. The term $\frac{w_L dV_L}{dU}$ is close to unity for low H_0/W_0-ratios and decreases for ratios above $1/2$, until reaching a contribution of around 20% for ratios of 4 and higher. This means that the decrease in total strain energy can predominantly be attributed to the volume reduction of the loaded region for low H_0/W_0-ratios. On the other hand, $\frac{V_L dw_L}{dU}$, shown in orange, increases for higher H_0/W_0-ratios, as the decrease in strain energy density within the loaded region becomes the more dominant contributor in this case.

Interestingly, for lower tearing energies, an initial decrease of Γ_{app}/Γ for H_0/W_0 between $1/4$ and 1 is observed (see EF-1 and EF-2 in Fig. 8), which means that Γ_{app} underestimates the effective tearing energy for such sample geometries. This behavior is associated with the fact that the mean strain energy density $\overline{w}$ is lower than the local strain energy density $w(x)$ in the central part of the sample (where crack propagation occurs), due to the lateral contraction at the free edges with increasing H_0/W_0-ratio. Fig. 11 shows that the increase of $w(x)$ across the center line of an unnotched sample in relation to the mean strain energy density $\overline{w}$ is particularly pronounced for quadratic sample geometries, such as $H_0/W_0 = 1$. In order to evaluate the influence of lateral contraction a linear elastic material model was implemented, using a Young's modulus $E = 0.098$ MPa, which corresponds to the stress–strain response of EF-1 at the respective fracture stretch, and a range of 0.5 to 0 was considered for the Poisson's ratio.

As can be seen in Fig. 12, for a Poisson's ratio $\nu = 0.5$ (incompressible behavior), Γ_{app}/Γ undergoes a distinct drop around $H_0/W_0 = 1/2$, while no change in Γ_{app}/Γ up to $H_0/W_0 = 2$ can be observed for $\nu = 0$.

Analogous calculations as for Ecoflex were performed with the material model representative of the soft biological tissue GC and considering two parameter sets GC-1 and GC-A, see Table 2. Note that for a non-incompressible material, like GC, the mode I fracture test cannot be referred to as a "pure shear" test, even for the case of very small H_0/W_0-ratios. In fact, due to the material behavior, the rate of out-of-plane contraction is not equal to the rate of elongation, and thus it does not lead to "pure shear" kinematics [34]. The curve for GC-A is similar to EF-A (see magenta and red curve in Fig. 13), while GC-1 (cyan curve) shows a much more pronounced underestimation of Γ_{app} than EF-1 (green curve).

Fig. 14 reports strain energy density values calculated at the center line of an unnotched sample. Indeed, the increase in energy density $w(x)$ towards the center ($x = 30$ mm) is much more distinctive for GC than for Ecoflex at lower fracture toughness. This is attributed to the highly contractile material behavior of GC, which might be more pronounced in the low strain regime. The case of GC-A, which is realistic in terms of tearing energy [16], leads to a reliable determination of Γ up to quadratic test pieces. Interestingly, for this case extraction of the stress intensity factor K_I from the stress nearfield leads also to a reliable determination of the corresponding tearing energy, see Appendix, Fig. A4.

4. Discussion

The mode I fracture test introduced by Rivlin and Thomas [10] is a well-established approach to determine the tearing energy of highly deformable materials. Our results show that mode I fracture tests conducted on sample geometries with large height-to-width ratios lead to a large overestimation of the tearing energy. However, an accurate estimation of the tearing energy can still be achieved for a surprisingly wide range of height-to-width ratios, even up to quadratic sample geometries in certain cases. In general, tougher materials with higher fracture stretches allow reliable measurements for sample geometries up to $H_0/W_0 = 1/2$. Brittle materials, here exemplified for the case $\lambda_c = 1.01$, permit even larger aspect ratios before overshooting, but lead to a non-negligible underestimation up to about 10% of the tearing energy for close-to-quadratic sample geometries. The latter is particularly pronounced in the case of large Poisson's ratios.

Two main factors influencing the error in the tearing energy determination were identified in terms of deviations with respect to the basic assumptions of the method proposed in [10]. For very low H_0/W_0-ratios the peculiarity of the mode I fracture test is the fact that the crack advances in a self-similar manner and thus the fracture process is not influenced by the crack length a. This is illustrated in Fig. 15, showing a fairly constant value of the relative far-field stretch in loading direction calculated for increasing crack size. In fact, in this case the governing dimension is the test piece height H_0, as the strain energy available for crack advance scales with H_0. This is confirmed in the present experiments and calculations, displaying a decreasing critical stretch λ_c for increasing H_0 values, see Fig. 6. When the H_0/W_0-ratio exceeds a critical limit, the self-similarity is lost, see Fig. 15, and the strain energy released upon crack advance depends on the crack length instead of the test piece height only.

In addition, the far-field strain energy decreases with crack advance as a consequence of the increased compliance of the test piece. The influence of these two factors is demonstrated in Fig. 9. The analysis demonstrates a compensation effect that induces a wider than

expected H_0/W_0-range leading to reliable tearing energy determination despite non-negligible lateral contraction, and thus deviation from a pure shear state.

The results of Fig. 8 can be represented also as a function of h_c/W_0, i.e. considering the deformed height at the onset of fracture. As shown in Fig. 16, the curves are shifted to the right by an amount that depends on the assumed fracture toughness. Interestingly, this representation brings the different curves closer, but still maintains a significant spread in the acceptability range, depending on the fracture toughness. In this case, the tearing energy overestimation is present for ratios above 1.5.

In view of the present results, the criteria previously proposed for H_0/W_0-ratios seem overconservative. In fact, previous investigations, see e.g. [11–13], propose upper bounds well below $1/2$ based on the observed deviation from a pure shear deformation state. In reality, reliable results might be obtained for larger ratios, depending on the magnitude of the fracture toughness and the constitutive behavior of the material considered. The present results confirm the validity of various studies conducted on elastomers and hydrogels, which have H_0/W_0-ratios in the range of 0.07 to 0.5 [17–23,39–41]. Mode I fracture experiments on highly stretchable materials, such as those reported in [17,18,23,39], might lead to very large fracture stretches λ_c. These cases cannot be directly compared with the present results, as the present calculations consider materials failing at much lower levels of deformation for comparable initial test piece geometries. In order to reproduce the test reported in [17], an additional calculation was performed with $H_0/W_0 = 1/2$ and failure at $h/W_0 = 9.8$. Using the Ecoflex constitutive model, the apparent tearing energy is only 8% larger than the one obtained through node opening simulations, indicating that the overestimation of Γ might still be in a tolerable range when the method of Rivlin and Thomas is applied for highly stretchable materials.

5. Conclusions

The influence of test piece geometry on the estimation of tearing energy in mode I fracture tests [10] was quantified. Test piece geometries with very large height-to-width ratios were found to result in gross overestimation of the tearing energy. The calculations show that the error depends on the magnitude of the tearing energy as well as on the constitutive behavior of the material considered. No generalized criterion can thus be proposed to maintain the error lower than a specific value.

For brittle materials, here exemplified for a critical stretch of 1.01, the tearing energy might be underestimated by up to 10% for aspect ratios close to a quadratic geometry. For cases with larger critical stretches, reliable values of the tearing energy were obtained for H_0/W_0 values up to $1/2$. Even in case of highly stretchable materials, with critical stretches in the order of 5 to 10, the tearing energy overestimation might still be in an acceptable range for initial height-to-width ratios of up to $1/2$. Thus, compared to the present results, criteria previously proposed in the literature seem overly conservative.

CRediT authorship contribution statement

E. Kahle: Writing – original draft, Visualization, Validation, Software, Methodology, Investigation, Data curation. **A.E. Ehret:** Writing - review & editing, Writing - original draft, Validation, Supervision, Methodology, Formal analysis. **E. Mazza:** Writing – review & editing, Writing – original draft, Validation, Supervision, Resources, Project administration, Methodology, Formal analysis, Conceptualization.

Declaration of Competing Interest

The authors declare that they have no known competing financial interests or personal relationships that could have appeared to influence the work reported in this paper.

Data availability

Data will be made available on request.

Acknowledgements

Appendix

Stress and stretch fields in the nearfield of the cracks

The local maximal principal first Piola-Kirchhoff stress P_{prin}^{max} was obtained from the results of the FE simulations for Ecoflex (case EF-2). Fig. A1 shows the maximum principal stress at a loading state for which the energy release rate obtained from node opening is the same as the experimentally determined value of tearing energy of Ecoflex. The far-field stress ($r > 0.1$mm) is lower for a larger aspect ratio, while the stress in the crack nearfield is identical.

As a next comparison, we extracted the maximal principal first Piola-Kirchhoff stress P_{prin}^{max}, and the corresponding maximal principal

nominal strain ε_{prin}^{max} from the simulations for Ecoflex (cases EF-1 and EF-A) and for GC (GC-1 and GC-A) at a stretch of 1.01 and 1.2, respectively. In Figs. A2 and A3 the corresponding values along the center line of the specimen are represented against the distance from the crack tip in the reference configuration. For larger far field strains, the strain nearfield deviates considerably from the $r^{-1/2}$ singularity expected from linear elastic fracture mechanics [9]. The stress nearfield, however, seems reasonably well approximated by the $r^{-1/2}$ singularity even for large tearing energies. This allows to evaluate the range of validity for the stress intensity factor [9]

$$K_I = P_{prin}^{max}\sqrt{2\pi r}$$

as a means of assessing the tearing energy.

Fig. A4 compares the prediction of the tearing energy based on the stress intensity factor and the energy release rate for the different ratios. To this end, the Young's modulus is approximated as the tangent of the first Piola-Kirchhoff stress vs. nominal strain response of the material at the respective stretch. For EF-1 and GC-1, the two predictions seem to agree well across the whole span of H_0/W_0-ratios despite the distinct material non-linearity of GC. For higher tearing energies, the K_I-based estimation of the tearing energy seems surprisingly accurate for both EF-A and GC-A. However, it needs be noted that due to the double logarithmic scale deviations between the two predictions are not clearly visible. Evaluation of the relative error of the K_I-based tearing energy estimate yields a maximum error of 52% for GC-1 and 80% for EF-A. Hence, the geometric non-linearity caused by large distortions in the nearfield, as in the case of EF-A, can be identified as the more dominant contributor to the discrepancy between small and large strain fracture analysis, in comparison to the material non-linearity.

Fig. A5 provides additional information on the evolution of the apparent tearing energy for different aspect ratios, at the example of Ecoflex set EF-2. The unsteady progression of ϕ' can be attributed to its dependence on the unloaded volume dV_L, which changes as a function of aspect ratio (black dotted line in Fig. A5). As illustrated with the sketches in Fig. A5, the green unloaded volume becomes larger than the dashed rectangle for increasing aspect ratios (H_0/W_0 close to $1/2$). For larger aspect ratios, the green area becomes smaller than the dashed rectangle, thus leading to a progressive decrease in ϕ'. Correspondingly, the relative reduction dw_L of strain energy density per unit volume of loaded region depends on the volume change of the loaded region, leading to a minimum of ϕ'' for the aspect ratio that maximizes ϕ'.

References

[1] Czech B, van Kessel R, Bauer P, Ferreira JA, Wattez A. Energy harvesting using Dielectric Elastomers. In: Proceedings of EPE-PEMC 2010–14th International Power Electronics and Motion Control Conference; 2010. https://doi.org/10.1109/EPEPEMC.2010.5606566.
[2] Chiba S, Waki M, Wada T, Hirakawa Y, Masuda K, Ikoma T. Consistent ocean wave energy harvesting using electroactive polymer (dielectric elastomer) artificial muscle generators. Appl Energy Apr. 2013;104:497–502. https://doi.org/10.1016/J.APENERGY.2012.10.052.
[3] Pelrine R., et al. Applications of dielectric elastomer actuators, Jul. 2001; 4329 (16): 335–349. doi: 10.1117/12.432665. https://doi.org/10.1117/12.432665.
[4] Curtis J, Colas A. In: Biomaterials Science. Elsevier; 2013. p. 1106–16.
[5] Necchi S, Molina D, Turri S, Rossetto F, Rietjens M, Pennati G. Failure of silicone gel breast implants: Is the mechanical weakening due to shell swelling a significant cause of prostheses rupture? J Mech Behav Biomed Mater Nov. 2011;4(8):2002–8. https://doi.org/10.1016/J.JMBBM.2011.06.019.
[6] Liebetraut P., Petsch S., Liebeskind J., Zappe H. "Elastomeric lenses with tunable astigmatism," Light: Science & Applications 2013 2:9, vol. 2, no. 9, pp. e98–e98, Sep. 2013, doi: 10.1038/lsa.2013.54.
[7] Yu B, Kang S-Y, Akthakul A, Ramadurai N, Pilkenton M, Patel A, et al. An elastic second skin. Nature Mater 2016;15(8):911–8.
[8] Andrews EH. A generalized theory of fracture mechanics. J Mater Sci 1974;9(6):887–94.
[9] Anderson TL. Fracture Mechanics : Fundamentals and Applications," Mar 2017. https://doi.org/10.1201/9781315370293.
[10] Rivlin RS, Thomas AG. Rupture of rubber. I. Characteristic energy for tearing. J Polym Sci Mar. 1953;10(3):291–318. https://doi.org/10.1002/POL.1953.120100303.
[11] Yeoh OH. Analysis of deformation and fracture of 'pure shear' rubber testpiece. Plast Rubber Compos Process Appl 2001;30(8):389–97. https://doi.org/10.1179/146580101101541787.
[12] Treloar LRG. Stress-strain data for vulcanised rubber under various types of deformation. Trans Faraday Soc Jan. 1944;40:59–70. https://doi.org/10.1039/TF9444000059.
[13] Hollenstein M, Ehret AE, Itskov M, Mazza E. A novel experimental procedure based on pure shear testing of dermatome-cut samples applied to porcine skin. Biomech Model Mechanobiol 2011;10(5):651–61.
[14] Bernardi L, Hopf R, Sibilio D, Ferrari A, Ehret AE, Mazza E. On the cyclic deformation behavior, fracture properties and cytotoxicity of silicone-based elastomers for biomedical applications. Polym Test Jul. 2017;60:117–23. https://doi.org/10.1016/J.POLYMERTESTING.2017.03.018.
[15] Bernardi L, Mazza E, Ehret AE. The effect of clamping conditions on tearing energy estimation for highly stretchable materials. Eng Fract Mech Feb. 2018;188: 300–8. https://doi.org/10.1016/J.ENGFRACMECH.2017.08.035.
[16] Bircher K., Zündel M., Pensalfini M., Ehret A.E., Mazza E. "Tear resistance of soft collagenous tissues," Nature Communications 2019 10:1, vol. 10, no. 1, pp. 1–13, Feb. 2019, doi: 10.1038/s41467-019-08723-y.
[17] You Y., Yang J., Zheng Q., Wu N., Lv Z., Jiang Z. "Ultra-stretchable hydrogels with hierarchical hydrogen bonds," Scientific Reports 2020 10:1, vol. 10, no. 1, pp. 1–8, Jul. 2020, doi: 10.1038/s41598-020-68678-9.
[18] Yang Y, Wang X, Yang F, Wang L, Wu D. Highly elastic and ultratough hybrid ionic-covalent hydrogels with tunable structures and mechanics. Adv Mater 2018; 30(18):1707071.
[19] Pharr M, Sun J-Y, Suo Z. Rupture of a highly stretchable acrylic dielectric elastomer. J Appl Phys 2012;111(10):104114.
[20] Zhang HJ, Sun TL, Zhang AK, Ikura Y, Nakajima T, Nonoyama T, et al. Tough physical double-network hydrogels based on amphiphilic triblock copolymers. Adv Mater 2016;28(24):4884–90.
[21] Sun TL, Kurokawa T, Kuroda S, Ihsan AB, Akasaki T, Sato K, et al. Physical hydrogels composed of polyampholytes demonstrate high toughness and viscoelasticity. Nature Mater 2013;12(10):932–7.
[22] Luo F, Sun TL, Nakajima T, Kurokawa T, Zhao Yu, Ihsan AB, et al. Crack blunting and advancing behaviors of tough and self-healing polyampholyte hydrogel. Macromolecules 2014;47(17):6037–46.
[23] Zhang W, Liu X, Wang J, Tang J, Hu J, Lu T, et al. Fatigue of double-network hydrogels. Eng Fract Mech 2018;187:74–93.

[24] Elmukashfi E. "An experimental method for estimating the tearing energy in rubber-like materials using the true stored energy," Scientific Reports 2021 11:1, vol. 11, no. 1, pp. 1–11, Aug. 2021, doi: 10.1038/s41598-021-95151-y.

[25] Corre T., Coret M., Verron E., Leblé B. "Non steady-state intersonic cracks in elastomer membranes under large static strain," Journal of Theoretical, Computational and Applied Mechanics, vol. Issue 2 | 2022, pp. 1–12, May 2021, doi: 10.46298/JTCAM.6906.

[26] Ahmad D, Sahu SK, Patra K. Fracture toughness, hysteresis and stretchability of dielectric elastomers under equibiaxial and biaxial loading. Polym Test Oct. 2019;79:106038. https://doi.org/10.1016/J.POLYMERTESTING.2019.106038.

[27] "Smooth-On, Inc. | Mold Making & Casting Materials | Rubbers, Plastics, Foams & More!" https://www.smooth-on.com/ (accessed Oct. 18, 2022).

[28] Hopf R, Bernardi L, Menze J, Zündel M, Mazza E, Ehret AE. Experimental and theoretical analyses of the age-dependent large-strain behavior of Sylgard 184 (10: 1) silicone elastomer. J Mech Behav Biomed Mater Jul. 2016;60:425–37. https://doi.org/10.1016/J.JMBBM.2016.02.022.

[29] Buerzle W, Mazza E. On the deformation behavior of human amnion. J Biomech Jul. 2013;46(11):1777–83. https://doi.org/10.1016/J.JBIOMECH.2013.05.018.

[30] Mauri A, Perrini M, Ehret AE, de Focatiis DSA, Mazza E. Time-dependent mechanical behavior of human amnion: Macroscopic and microscopic characterization. Acta Biomater 2015;11(1):314–23. https://doi.org/10.1016/J.ACTBIO.2014.09.012.

[31] Perrini M, et al. Mechanical and microstructural investigation of the cyclic behavior of human amnion. J Biomech Eng Jun. 2015;137(6). https://doi.org/10.1115/1.4030054.

[32] Bircher K, Ehret AE, Mazza E. Mechanical characteristics of bovine glisson's capsule as a model tissue for soft collagenous membranes. J Biomech Eng 2016;138 (8):Aug. https://doi.org/10.1115/1.4033917.

[33] Steck D, Qu J, Kordmahale SB, Tscharnuter D, Muliana A, Kameoka J. Mechanical responses of Ecoflex silicone rubber: Compressible and incompressible behaviors. J Appl Polym Sci 2019;136(5):47025.

[34] Ogden R.W. "Large deformation isotropic elasticity – on the correlation of theory and experiment for incompressible rubberlike solids," Proceedings of the Royal Society of London. A. Mathematical and Physical Sciences, vol. 326, no. 1567, pp. 565–584, Feb. 1972, doi: 10.1098/RSPA.1972.0026.

[35] Rubin MB, Bodner SR. A three-dimensional nonlinear model for dissipative response of soft tissue. Int J Solids Struct Sep. 2002;39(19):5081–99. https://doi.org/10.1016/S0020-7683(02)00237-8.

[36] Mauri A, Ehret AE, de Focatiis DSA, Mazza E. A model for the compressible, viscoelastic behavior of human amnion addressing tissue variability through a single parameter. Biomech Model Mechanobiol Aug. 2016;15(4):1005–17. https://doi.org/10.1007/S10237-015-0739-0/FIGURES/7.

[37] Begley JA, Landes JD. The J integral as a fracture criterion. Sep 1971.

[38] Naït-Abdelaziz M, Zaïri F, Qu Z, Hamdi A, Aït Hocine N. J integral as a fracture criterion of rubber-like materials using the intrinsic defect concept. Mech Mater 2012;53:80–90.

[39] Zhang M, Yu J, Shen K, Wang R, Du J, Zhao X, et al. Highly stretchable nanocomposite hydrogels with outstanding antifatigue fracture based on robust noncovalent interactions for wound healing. Chem Mater 2021;33(16):6453–63.

[40] Fan W, Wang Y, Cai S. Fatigue fracture of a highly stretchable acrylic elastomer. Polym Test Aug. 2017;61:373–7. https://doi.org/10.1016/J.POLYMERTESTING.2017.06.005.

[41] Sun J-Y, Zhao X, Illeperuma WRK, Chaudhuri O, Oh KH, Mooney DJ, et al. Highly stretchable and tough hydrogels. Nature 2012;489(7414):133–6.